ELECTRONIC SUPPLEMENTARY INFORMATION

Improving the efficiency and stability of perovskite solar cells using π-conjugated aromatic additives with differing hydrophobicities

Ran Wang[a],*, Amal Altujjar[a], Nourdine Zibouche[b,c], Xuelian Wang [a], Ben F. Spencer[a,d], Zhenyu Jia [a], Andrew G. Thomas[a,d], Muhamad Z. Mokhtar[a,e], Rongsheng Cai[a], Sarah J. Haigh[a], Jennifer M. Saunders [a], M. Saiful Islam[f] and Brian R. Saunders[a],*

a) Department of Materials, University of Manchester, MECD(A), Manchester, M1 7HL, UK.

b) Department of Chemistry, University of Bath, Bath, BA2 7AY, UK.

c) Department of Chemistry, Lancaster University, Lancaster, LA1 4YB, UK

d) Photon Science Institute, The Henry Royce Institute, University of Manchester, Manchester, M13 9PL, UK

e) Department of Water and Environmental Engineering, Faculty of Civil Engineering, Universiti Teknologi Malaysia, 81310 Johor Bahru, Johor, Malaysia.

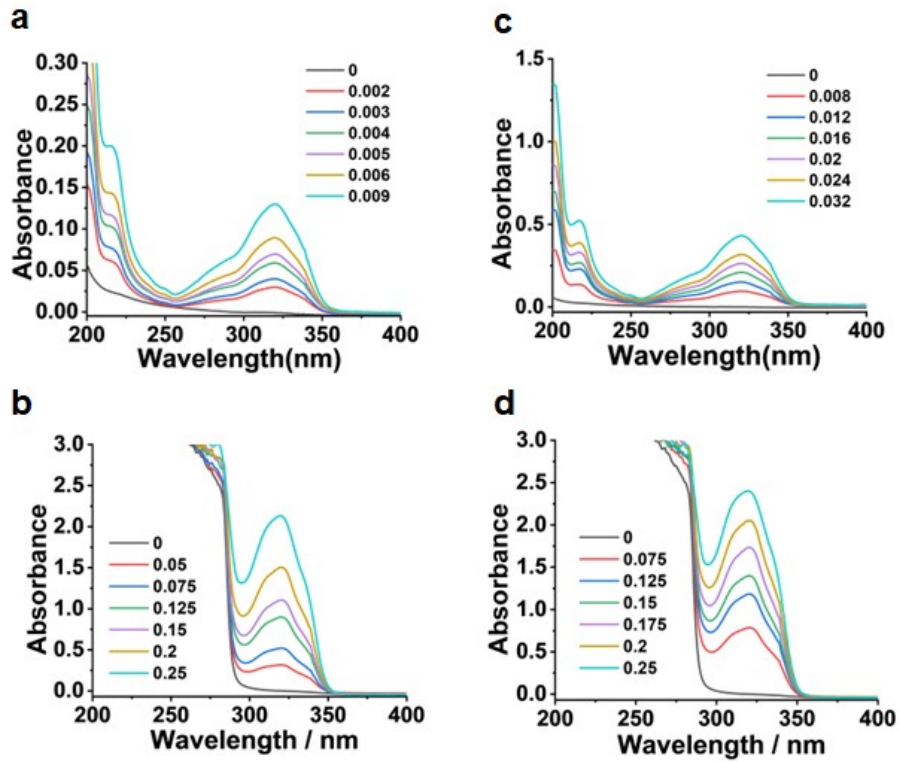f) Department of Materials, University of Oxford, Oxford, OX1 3PH, UK.

Fig. S1. UV-visible spectra for construction of calibration curves (Fig. S2). Various concentrations of CMA in **(a)** water and **(b)** CBZ. UV-visible spectra are also shown for CHE in **(c)** water or **(d)** CBZ. The concentrations (M) used are shown in the legends.
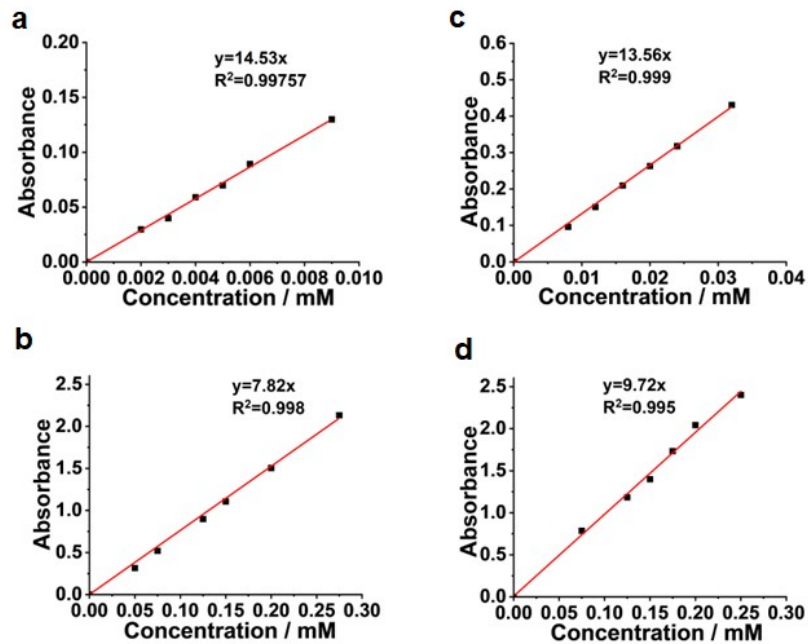

Fig. S2. Absorbance vs. concentration plots for CMA in **(a)** water or **(b)** CBZ as well as CHE in **(c)** water or **(d)** CBZ. The data are taken from Fig. S1.

Ruling out free-radical polymerization of CMA

Several groups have reported that vinyl-containing molecules can polymerize within perovskite films during preparation[1, 2]. Therefore, ^{1}H NMR spectra were measured from CMA and CHE before and after the heat treatment at 55 °C for 2 h (see Fig. S3). (The spectra for CHE are used as a control.) The ^{1}H NMR spectra showed no change in the CMA methacrylate group content. Hence, CMA did not undergo polymerization under these conditions. It is noted that these model conditions do not replicate those in a working device where applied bias and free electrons may affect reactivity. Nevertheless, based on the available evidence we propose that CMA did not undergo polymerization when included in the perovskite films in this study and behaved as a single molecule additive. This conclusion is expected because (1) our precursor solutions and films were prepared in low oxygen environments, (2) there were no added free-radical initiators present and (3) low additive concentrations were used. Such conditions do not favour free-radical polymerization.

The ^{1}H NMR spectra discussed above provide useful characterization data for the CAAs studied in this work. To complete the characterizations of CMA and CHE, ^{13}C NMR spectra were also measured (see Fig. S4). These spectra confirm the identities of each additive.
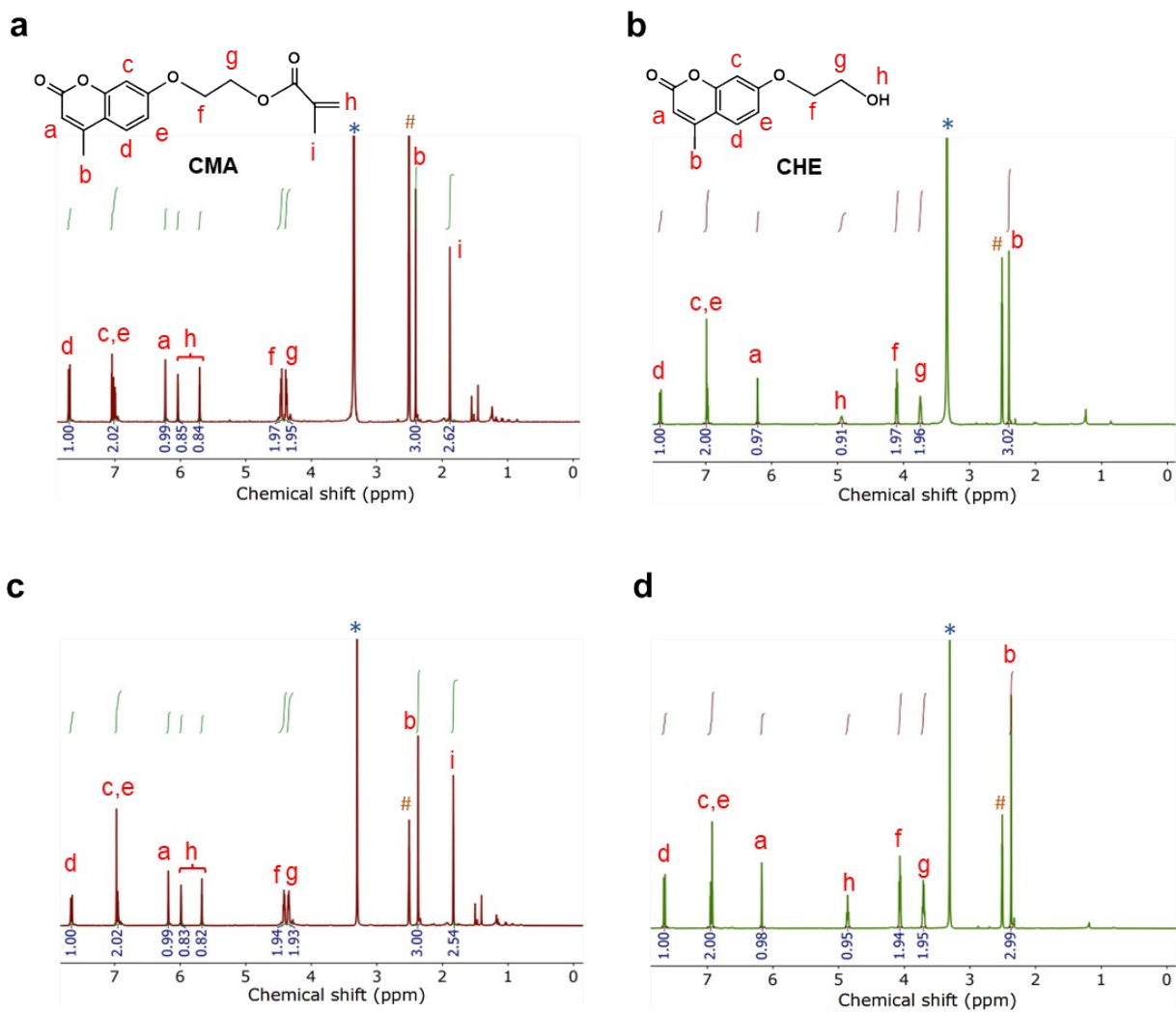
Fig. S3. ^{1}H NMR spectra for CMA (**(a)** and **(c)**) and CHE (**(b)** and **(d)**). The spectra shown in (a) and (b) were obtained in DMSO-d$_6$ before heating. The spectra shown in (c) and (d) were measured in DMSO-d$_6$ solutions containing PbI$_2$ after heating at 55 °C for 2 h.

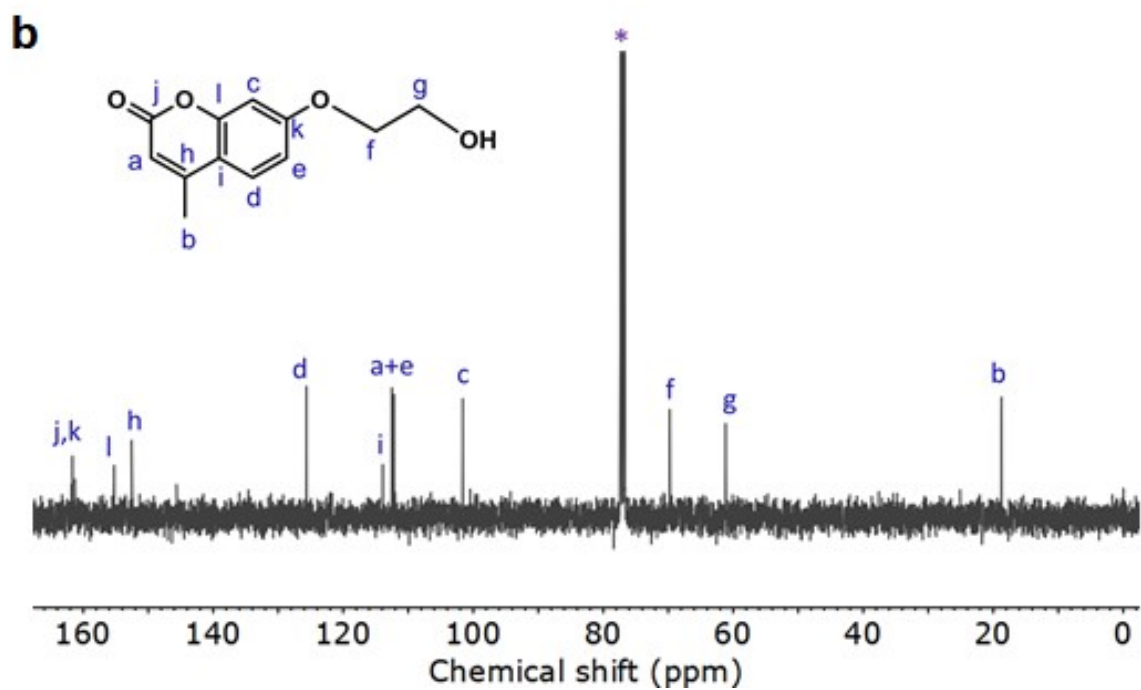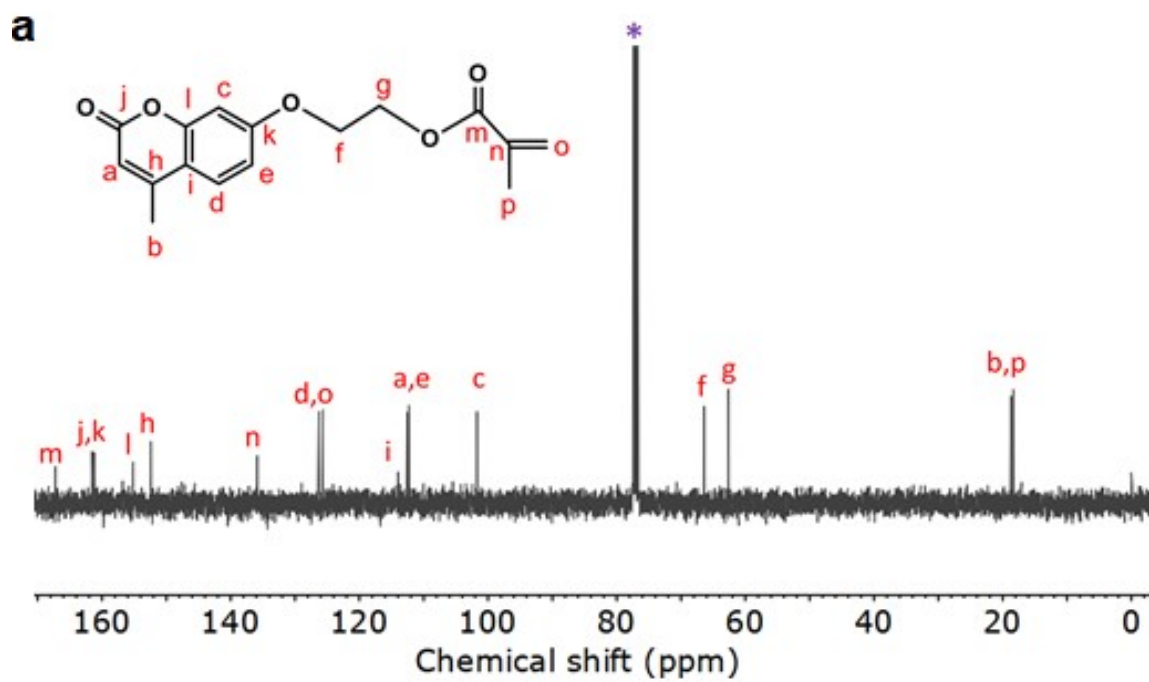**Fig. S4.** ^{13}C NMR spectra for **(A)** CMA and **(B)** CHE in CDCl$_3$.
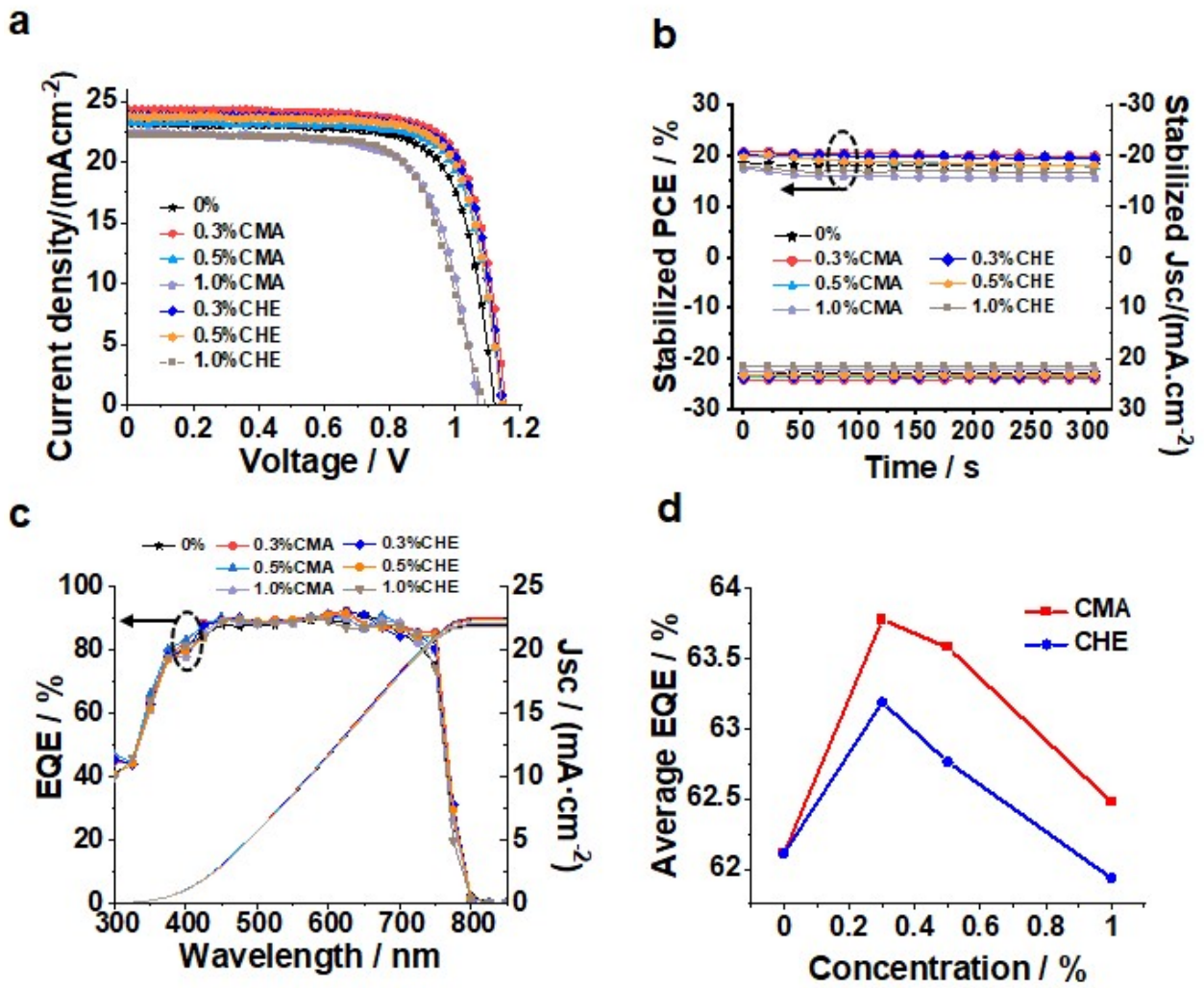
Fig. S5. (a) *J-V* curves for champion devices. **(b)** Stabilized power output and photocurrent for the devices studied. **(c)** EQE spectra for the systems. The integrated short-circuit current density data are also shown. **(d)** Average EQE values obtained from (c).

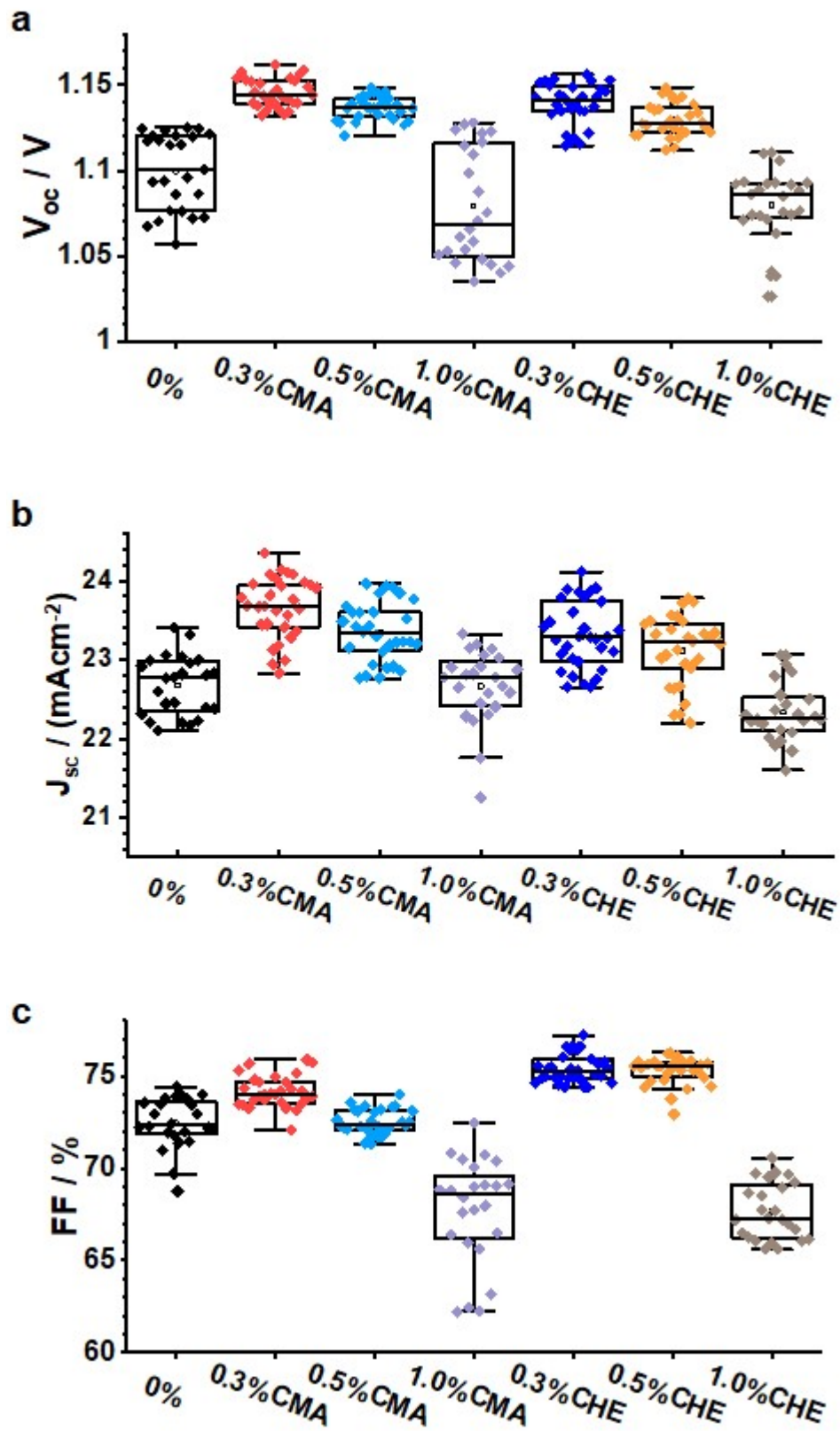**Fig. S6.** Box plots showing the measured **(a)** V_{oc}, **(b)** J_{sc} and **(c)** FF values for the PSCs studied.
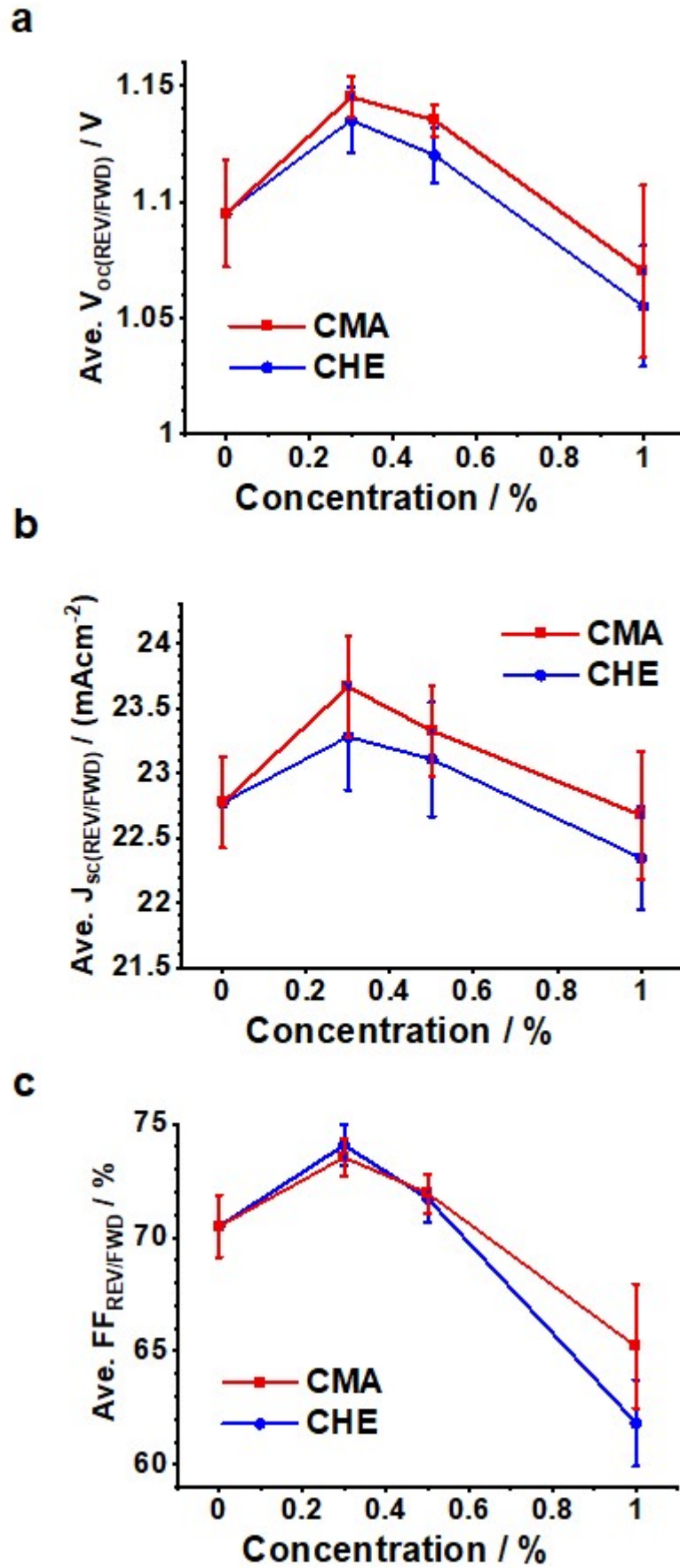
Fig. S7. Average of reverse and forward sweep **(a)** V_{oc}, **(b)** J_{sc} and **(c)** FF values measured for the devices.
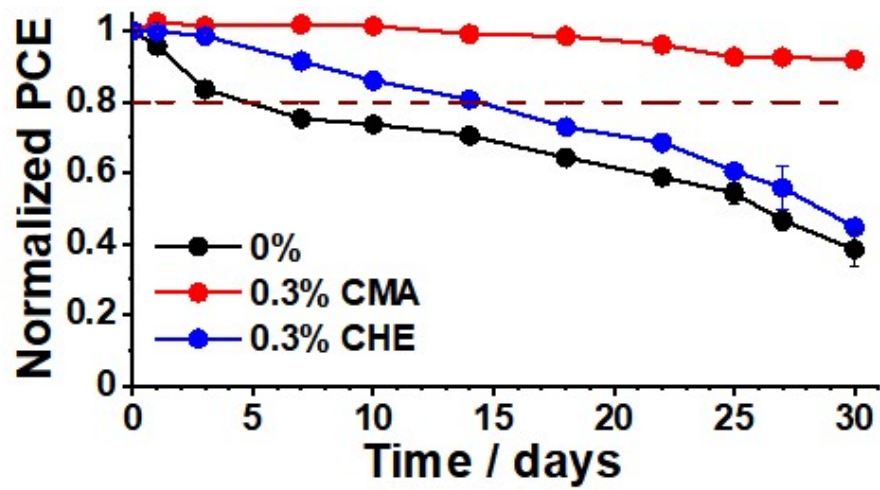
Fig. S8. Thermal stability of unencapsulated devices stored at 85 °C and 45% RH in the dark. The error bars are smaller than many of the data points.
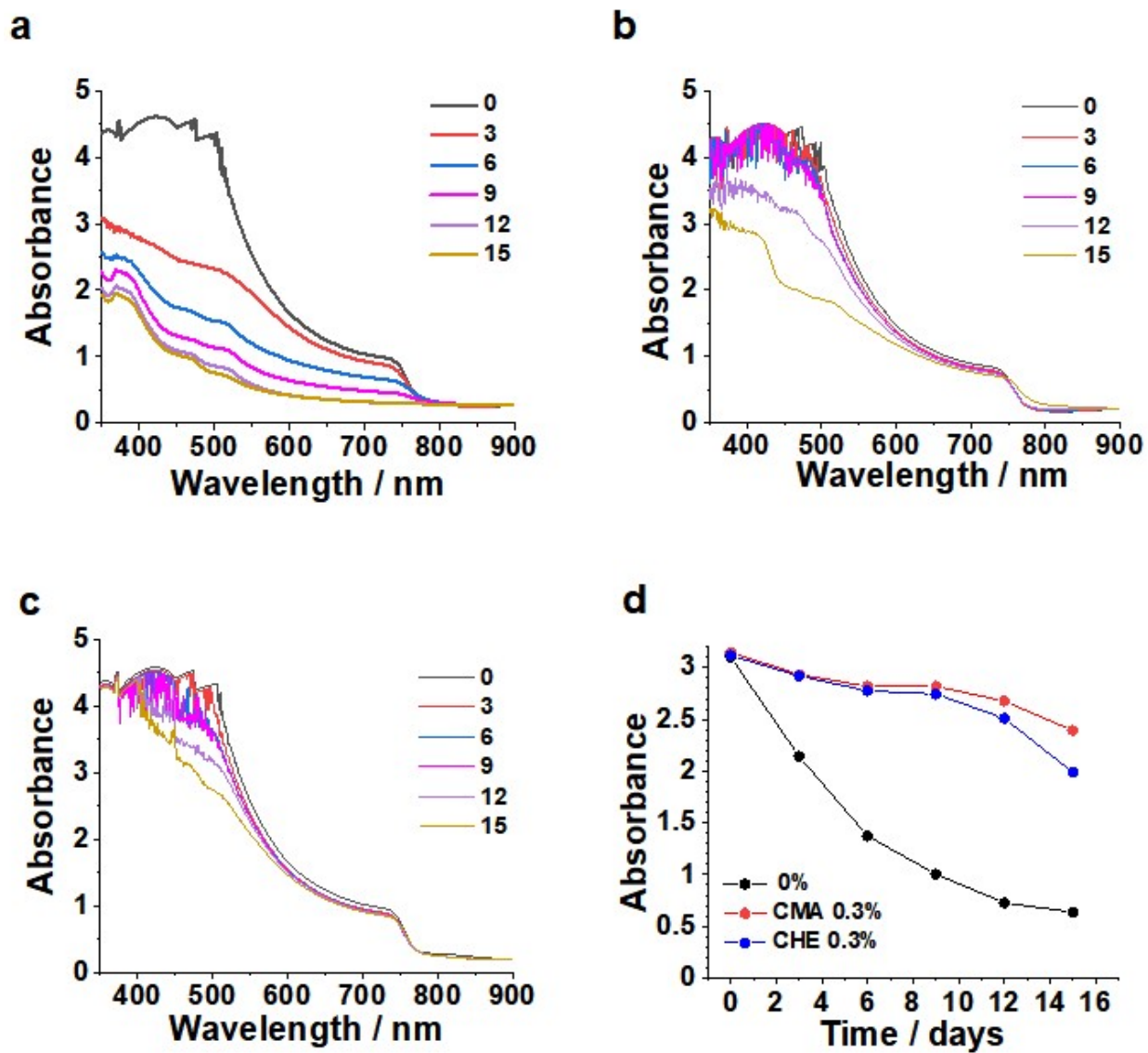
Fig. S9. UV-visible spectra recorded at different times for perovskite films prepared using **(a)** 0%, **(b)** 0.3% CHE and **(c)** 0.3% CMA stored at 90% RH and 25 °C. The time periods in days are shown in the legends. **(d)** Absorbance values at 530 nm taken from the spectra shown in (a) – (c).
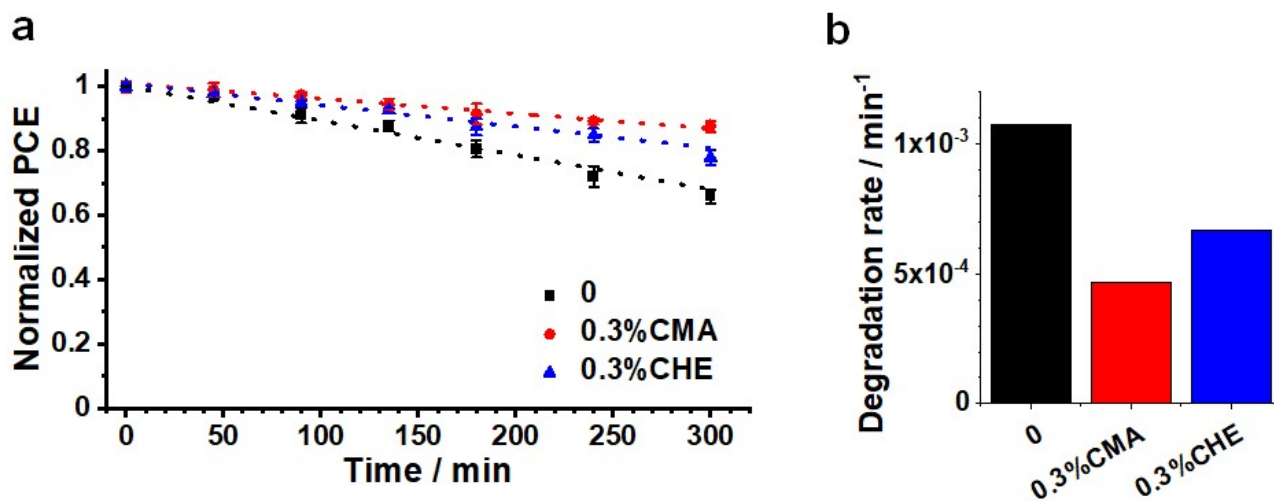
Fig. S10. (a) Light soaking stability measurements for 0%, 0.3% CMA and 0.3% CHE devices under 1 Sun illumination and 45% RH at 30 °C without encapsulation. **(b)** Degradation rates using the gradients from the linear fits shown in (a) for each of the systems. The degradation rates increased in the order: 0.3% CMA < 0.3% CHE < 0% (control).
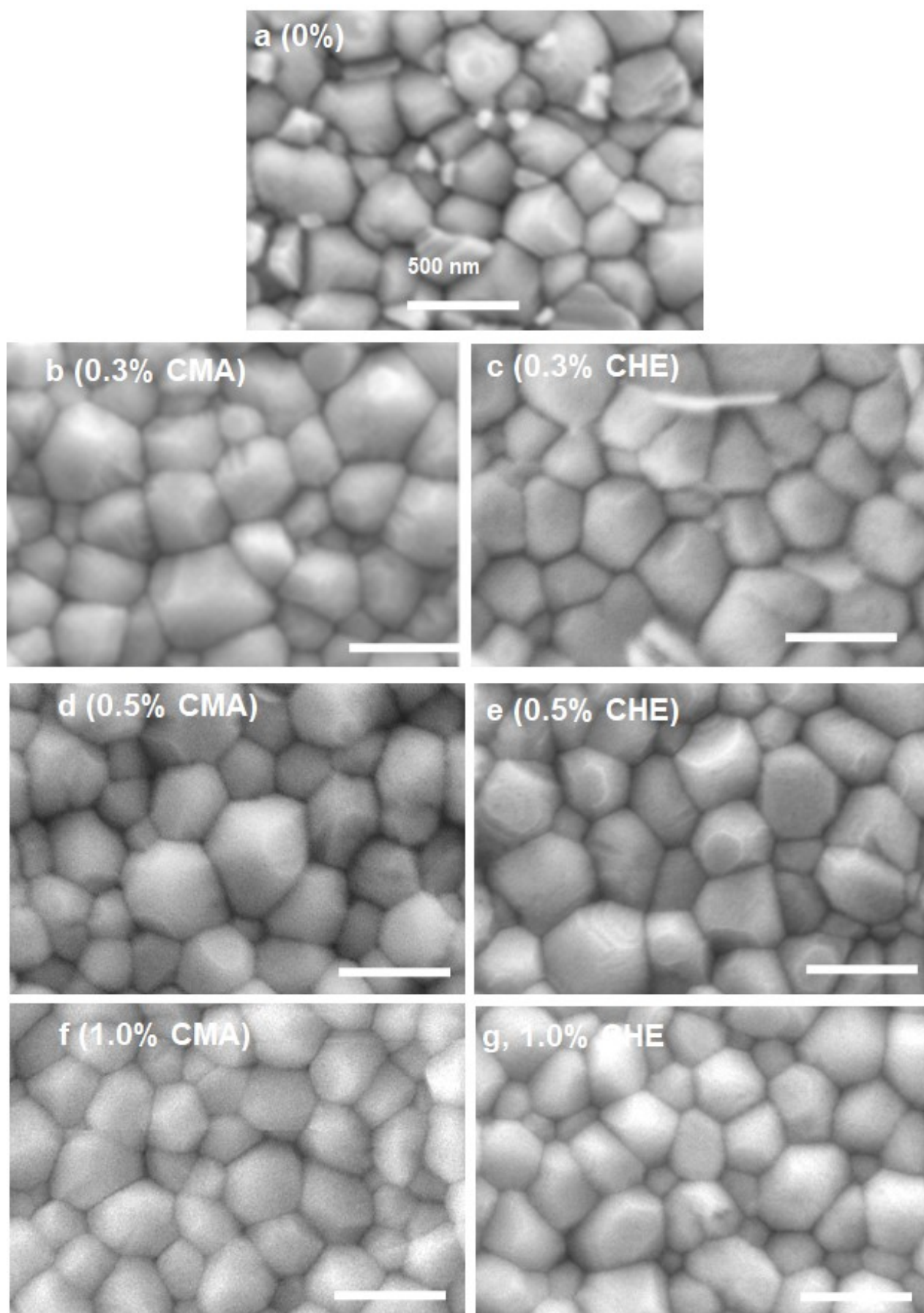
Fig. S11. **((a) – (g))** Top view SEM images for perovskite films prepared using CMA or CHE. The grain size distributions for each sample are shown in Fig. S13.
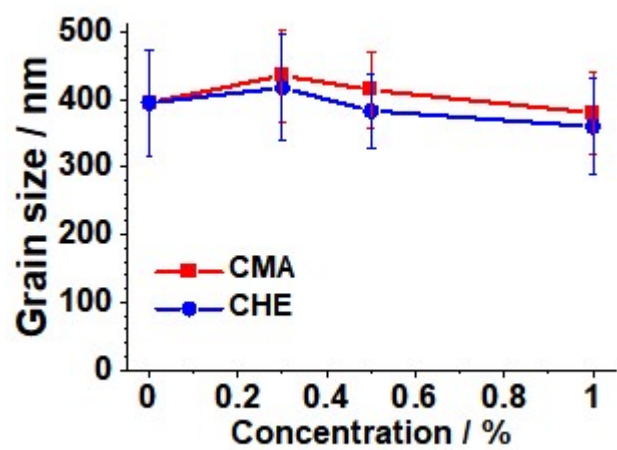
Fig. S12. Grain size variation with concentration of CMA or CHE used for perovskite film preparation.
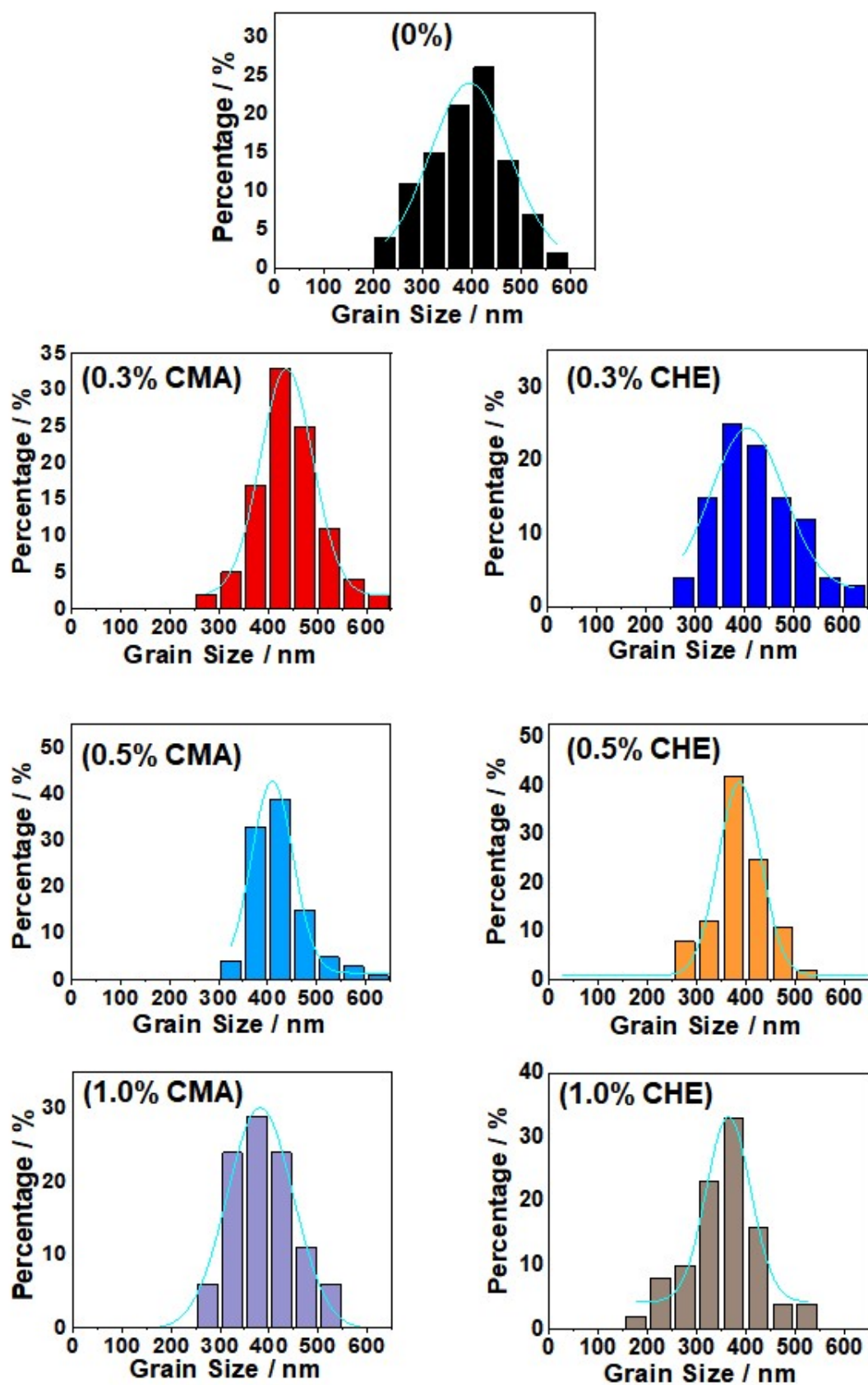
Fig. S13. Grain-size distributions measured from SEM images (Fig. S11) for perovskite films prepared using various concentrations of CMA or CHE.

a (0%)

Au
Spiro

Perovskite

SnO$_2$
ITO

500 nm

b(0.3% CMA)

c (0.3% CHE)

d (0.5% CMA)

e (0.5% CHE)

f (1.0% CMA)

g (1.0% CHE)
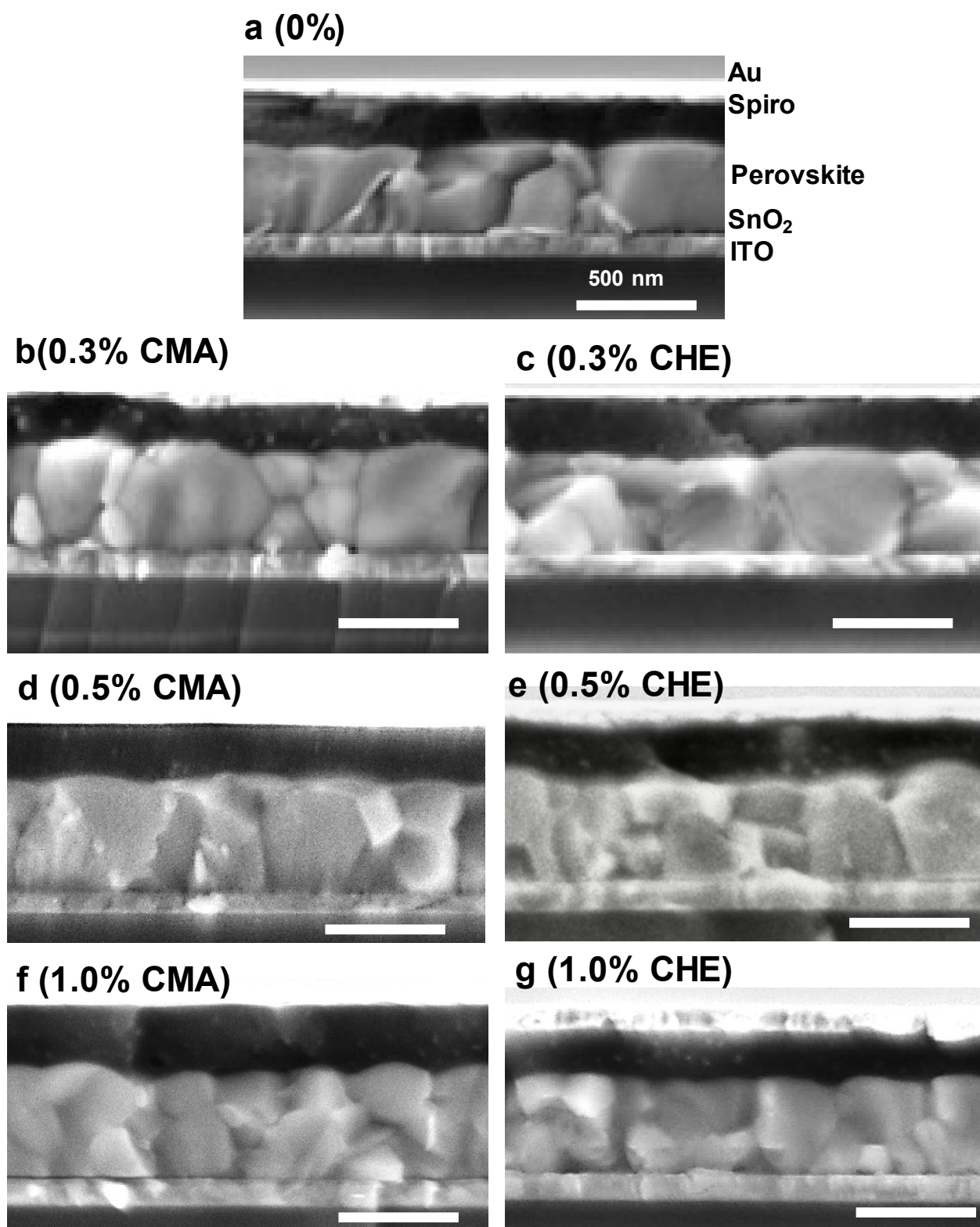
Fig. S14. **((a) – (g))** SEM images of cross-sections from PSCs prepared using different concentrations of CMA or CHE (shown).
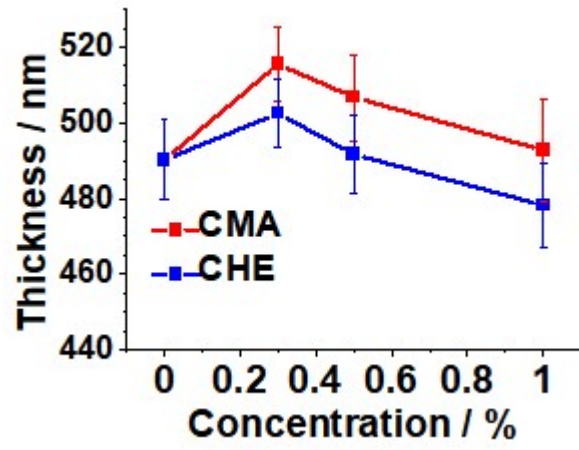
Fig. S15. Average thickness of the perovskite layers.
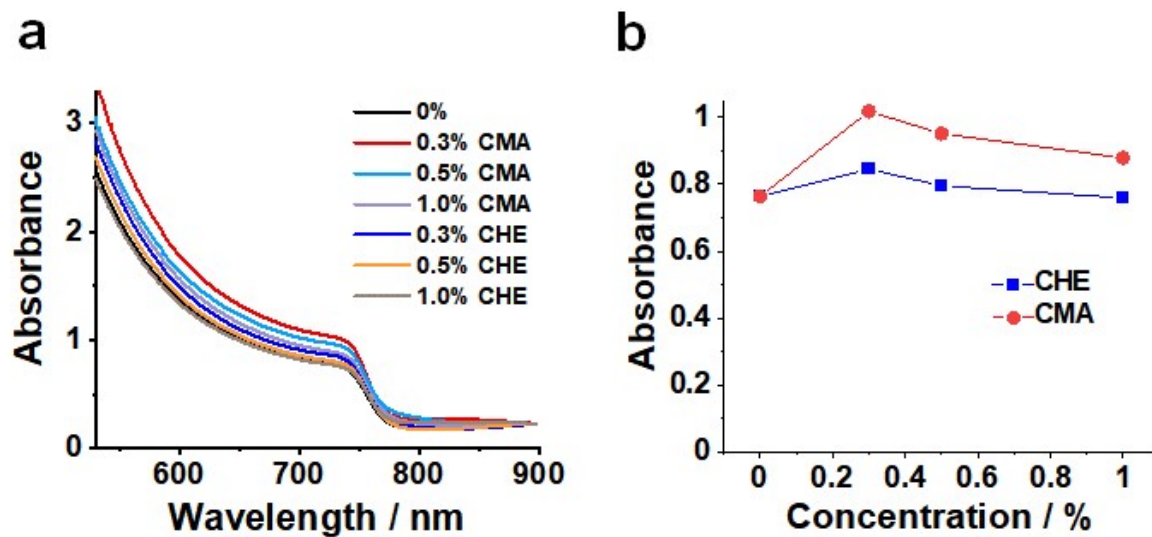
Fig. S16. (a) UV-visible spectra for perovskite films prepared using different concentrations of CHE or CMA (legend). **(b)** Absorbance measured at 733 nm as a function of CMA or CHE concentration. The data were taken from the spectra in (a).
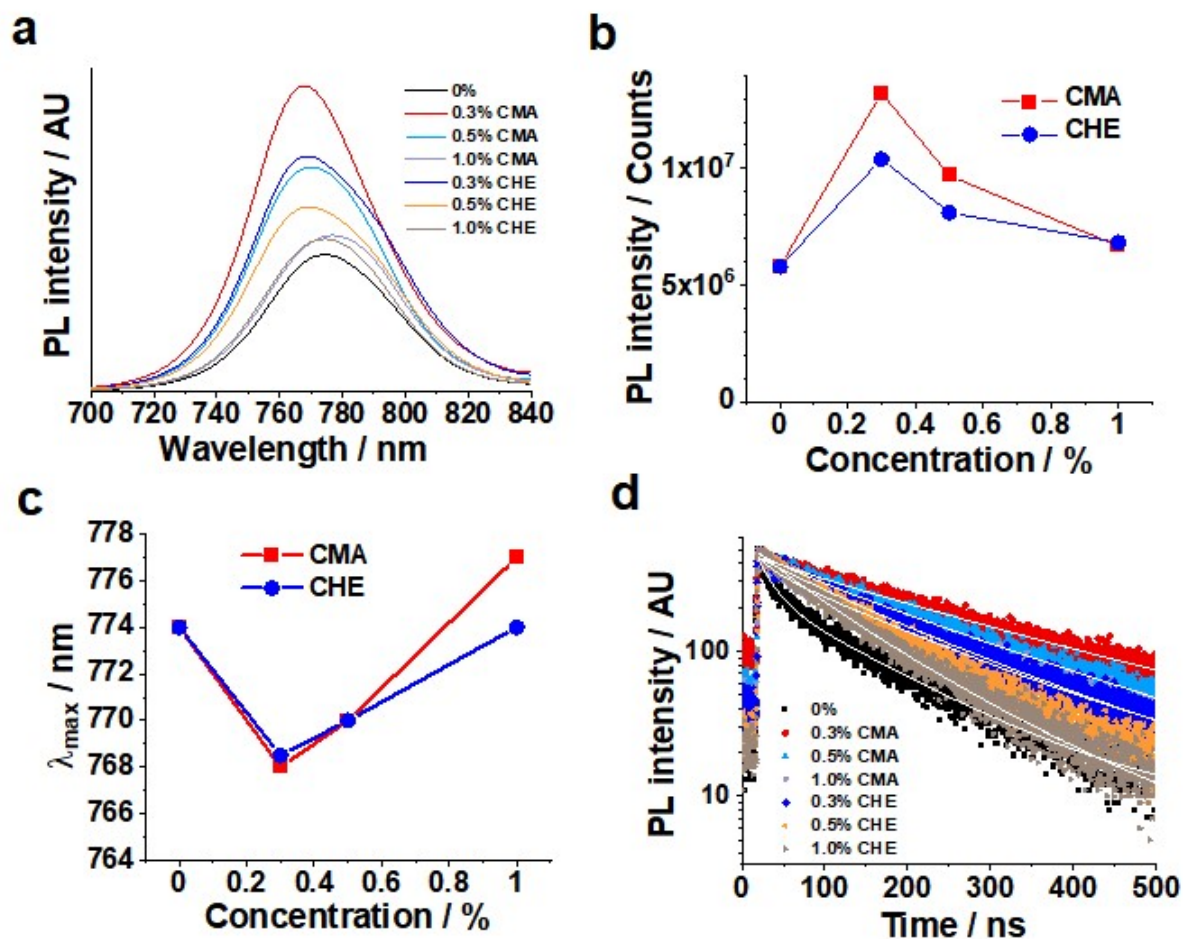
Fig. S17. (a) Steady-state PL spectra for all of the systems studied (see legend). **(b)** Maximum PL intensity for each system. **(c)** Variation of the wavelength at maximum PL intensity with concentration of CMA or CHE. The data shown in (b) and (c) are taken from the spectra shown in (a). **(d)** TRPL data and fits according to equation 1 for the perovskite films. The substrate used for all of the PL measurements was ITO/SnO$_2$.
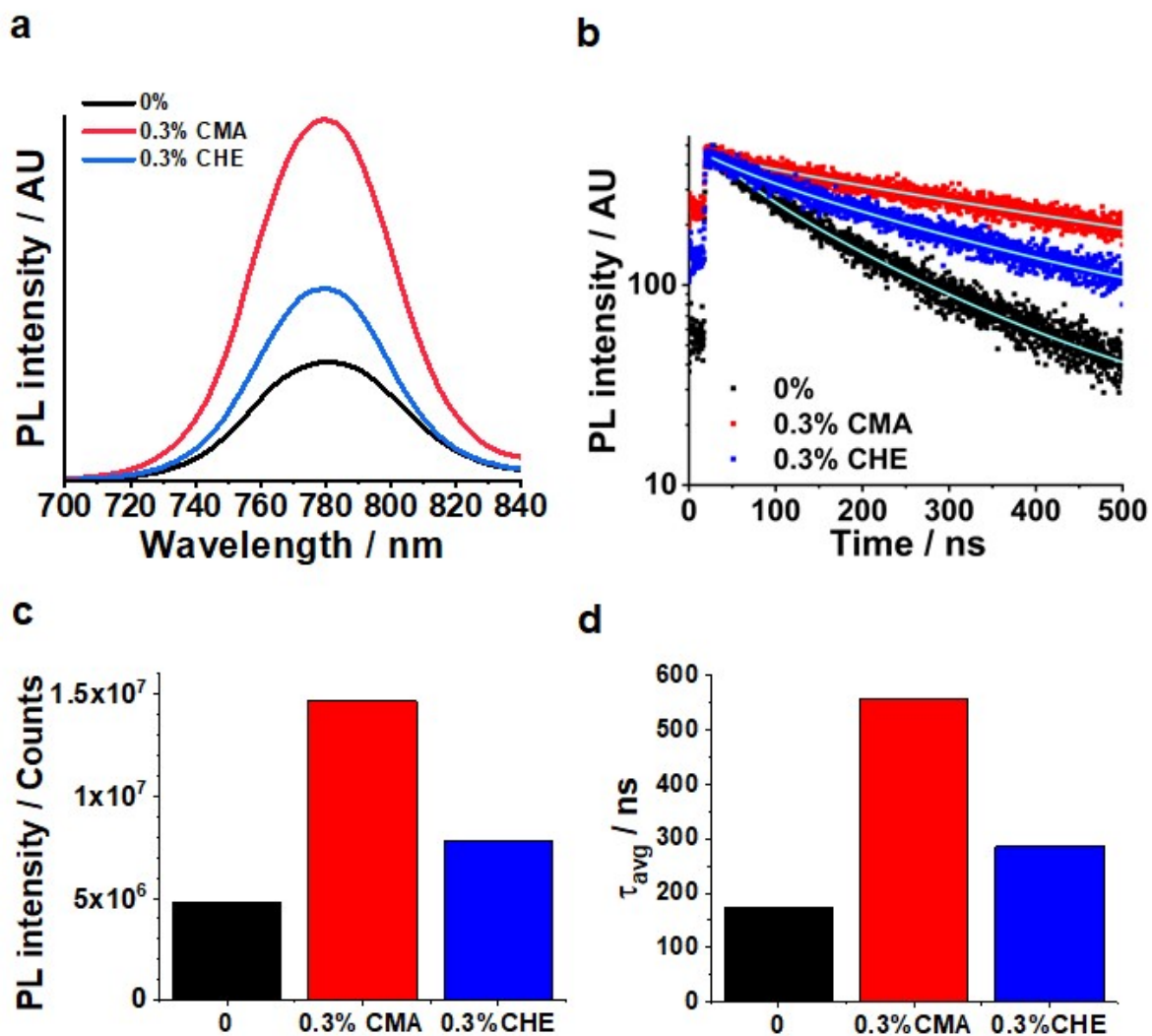
Fig. S18. (a) Steady-state and **(b)** time-resolved PL spectra for selected systems deposited on glass with light incident from the glass side. **(c)** Maximum PL intensity values from (a). **(d)** Average carrier lifetime values from fitting the data in (b) using equations (1) and (2). The values for the fitting parameters are shown in Table S3.
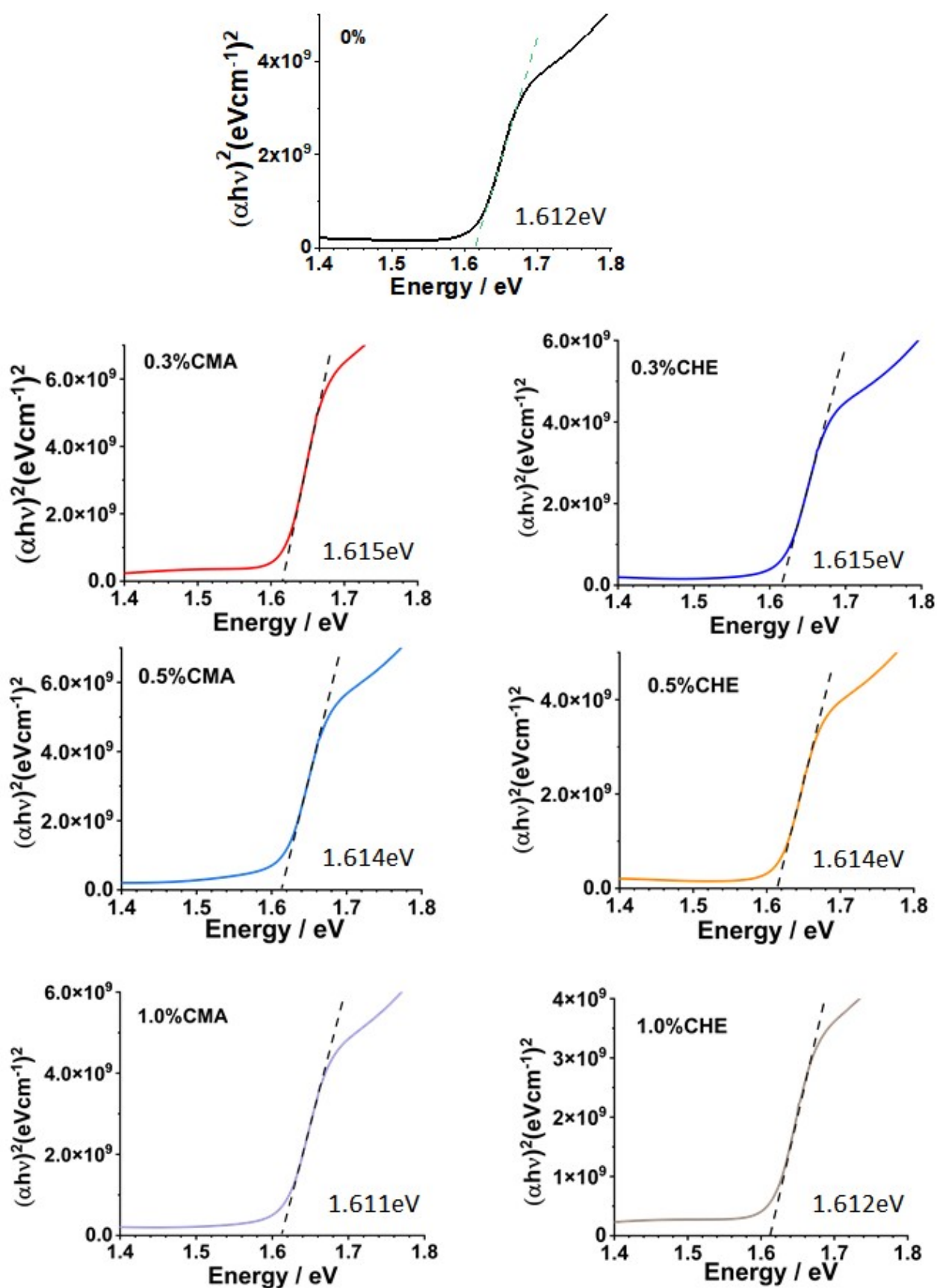
Fig. S19. Tauc plots for the perovskite films in this study. The data were obtained from Fig. S16a. The values for the band gap (E_g) are obtained from the intersection with the x-axis.

Configuration I

Configuration II

Configuration III

Configuration IV

Configuration V
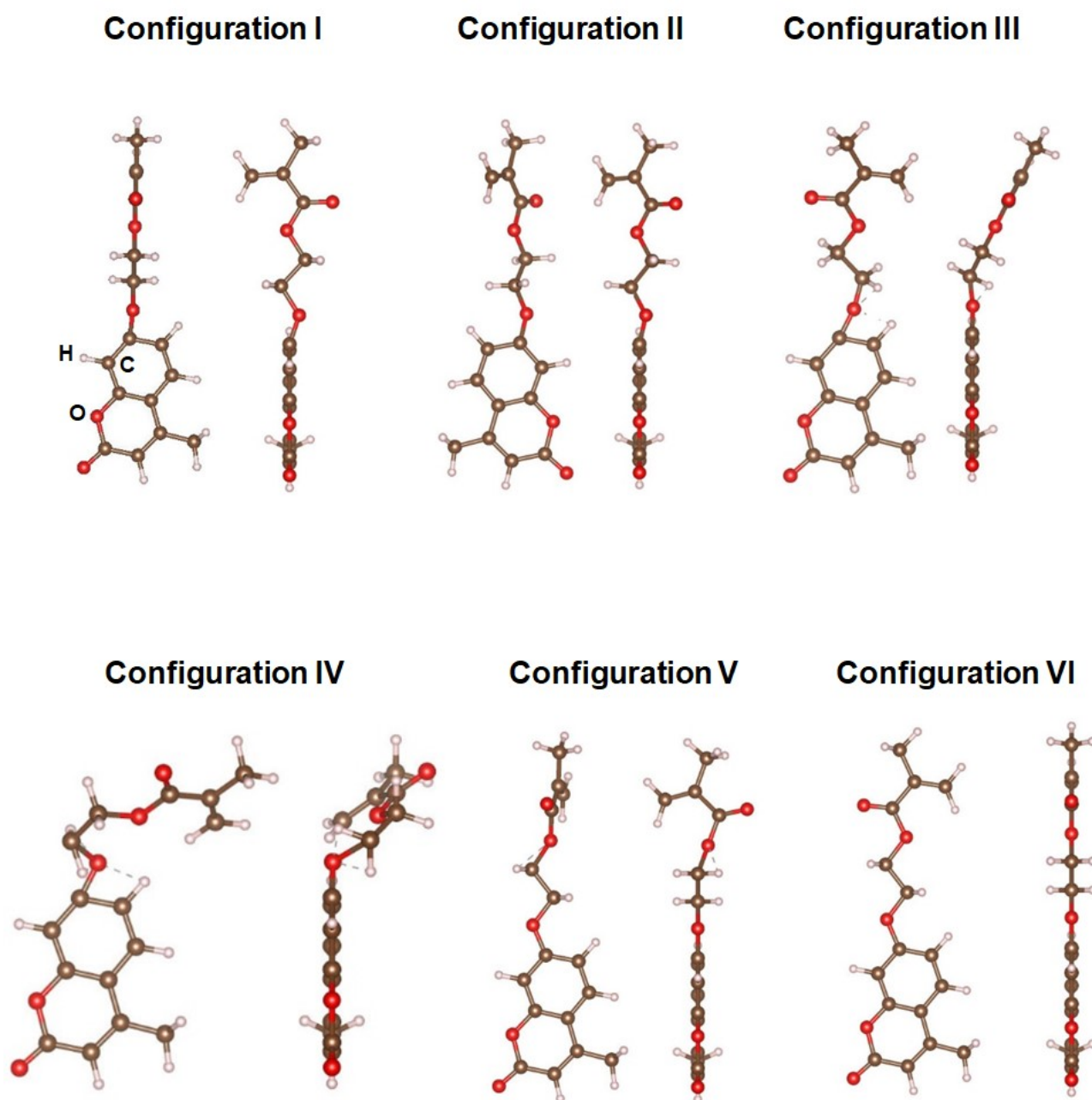
Configuration VI

Fig. S20. The six configurations of CMA *before* binding to the perovskite surface considered in this study. The relative energies for these conformations are shown in Table S4. Configuration VI is the most energetically favorable and was subsequently used to study the interaction with perovskite surfaces.
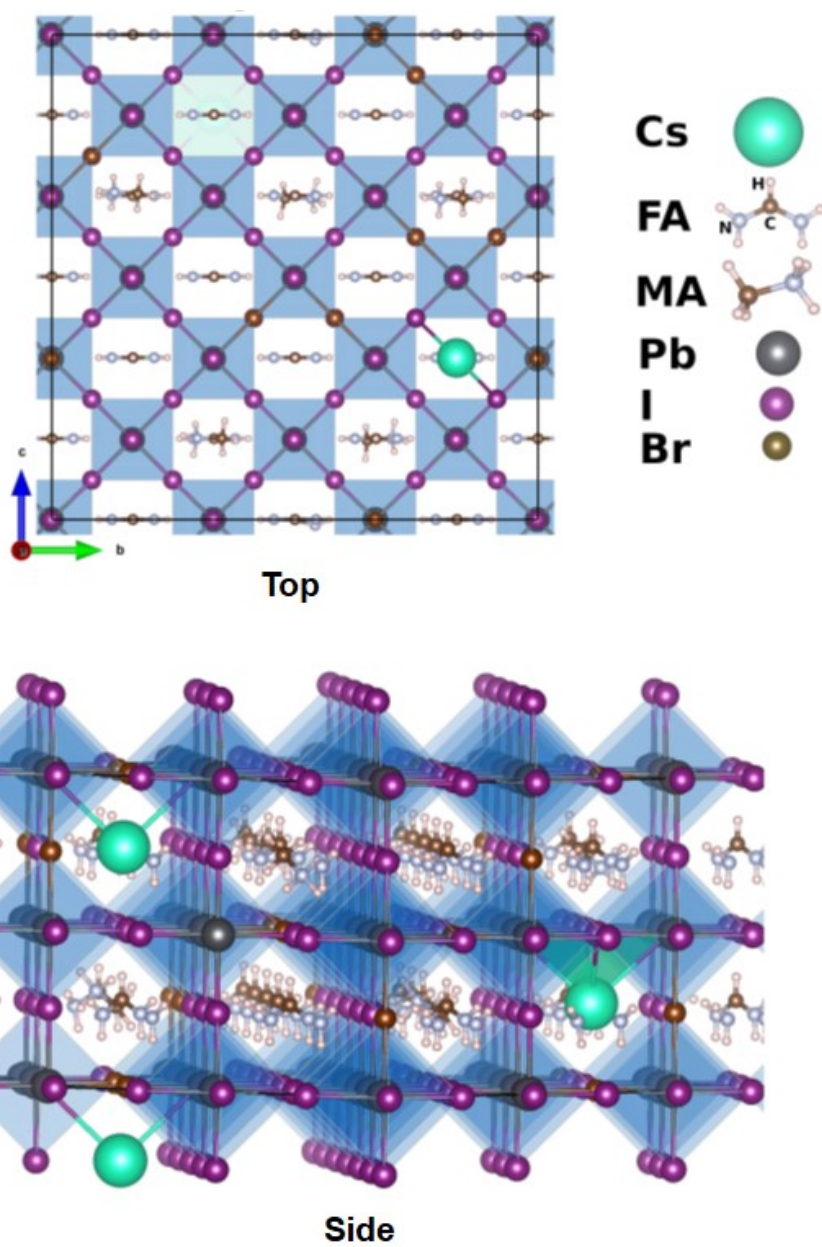
Fig. S21. Top and side views of the bulk structure model of $Cs_{0.05}(FA_{0.85}MA_{0.15})_{0.95}Pb(I_{0.85}Br_{0.15})_3$.
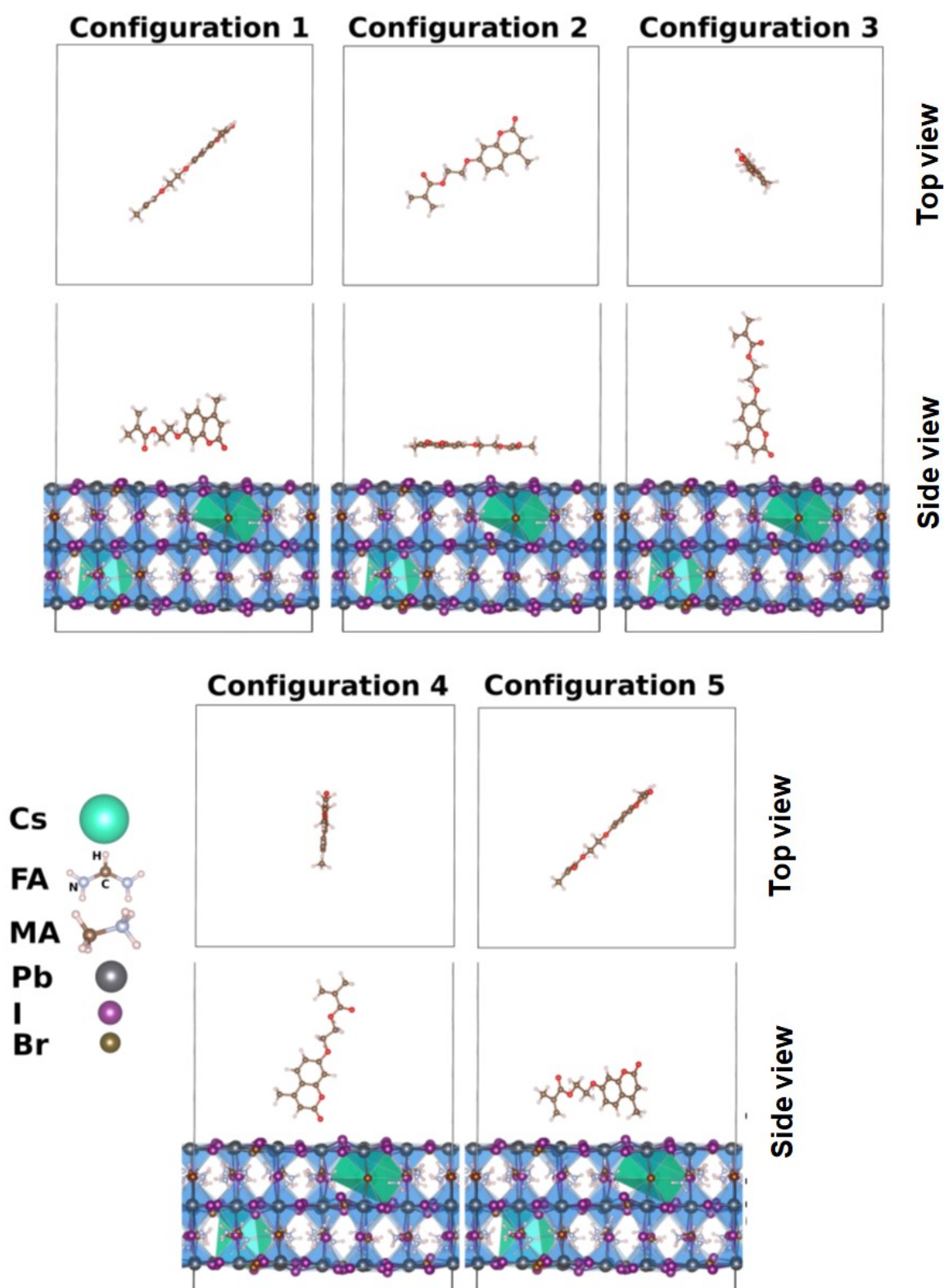
Fig. S22. The five configurations of each coumarin on each perovskite surface considered in this study. The figures show examples of CMA on the PbX terminated surface. The same configurations were considered on the AX terminated surface for CMA and CHE, which gives 20 configurations. The perovskite surface is removed in the top view panels for clarity. These configurations are chosen to cover most of possible arrangements of the coumarins that will interact with the perovskite surfaces.
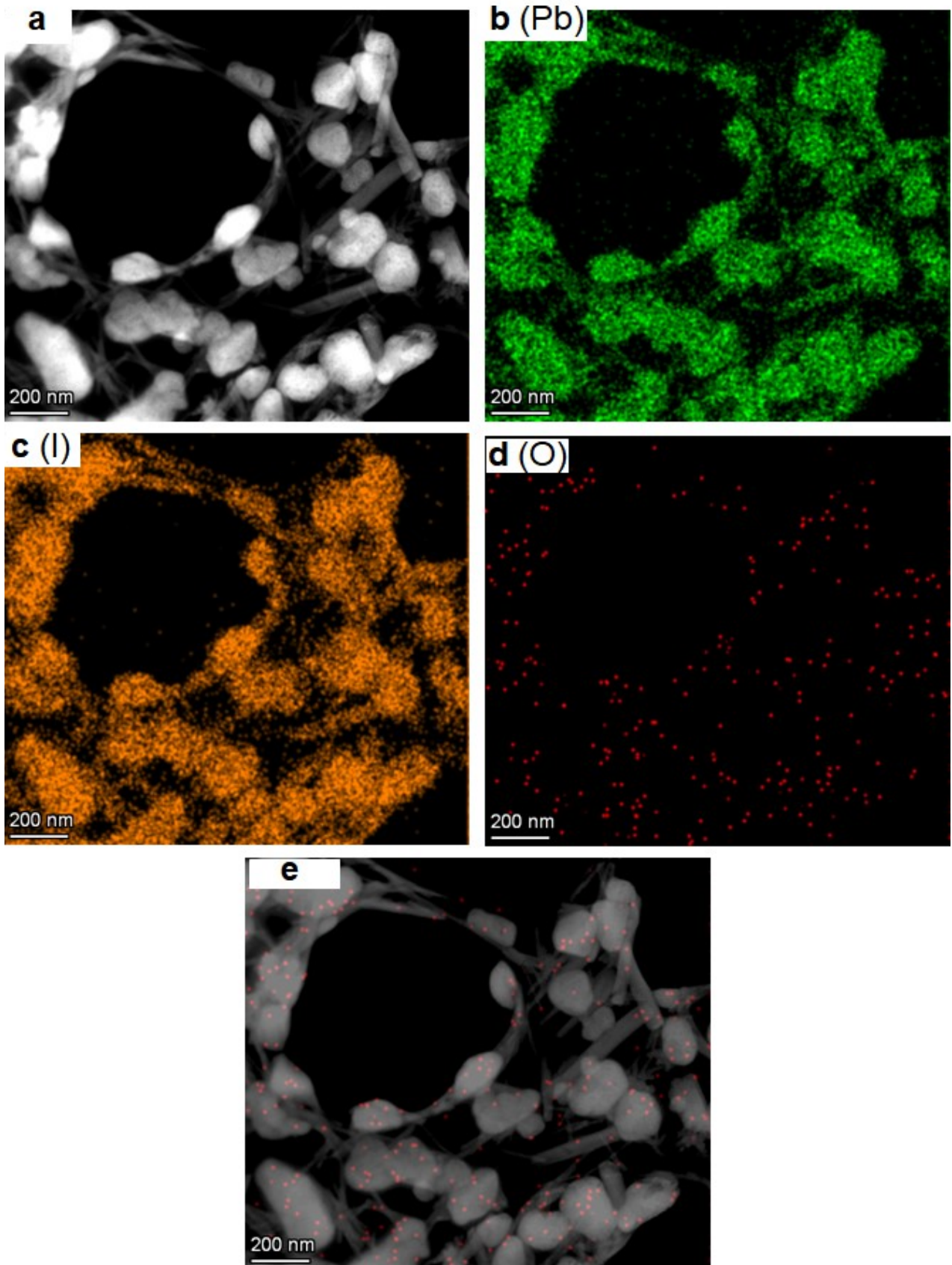
Fig. S23. HAADF STEM **(a)** and STEM-EDS data (**b - d**) measured for perovskite grains deposited from a dilute perovskite solution (0.28 M) containing 1% CMA. **(e)** A composite colour map that overlays the oxygen elemental STEM-EDS data (d) with the STEM image (a).
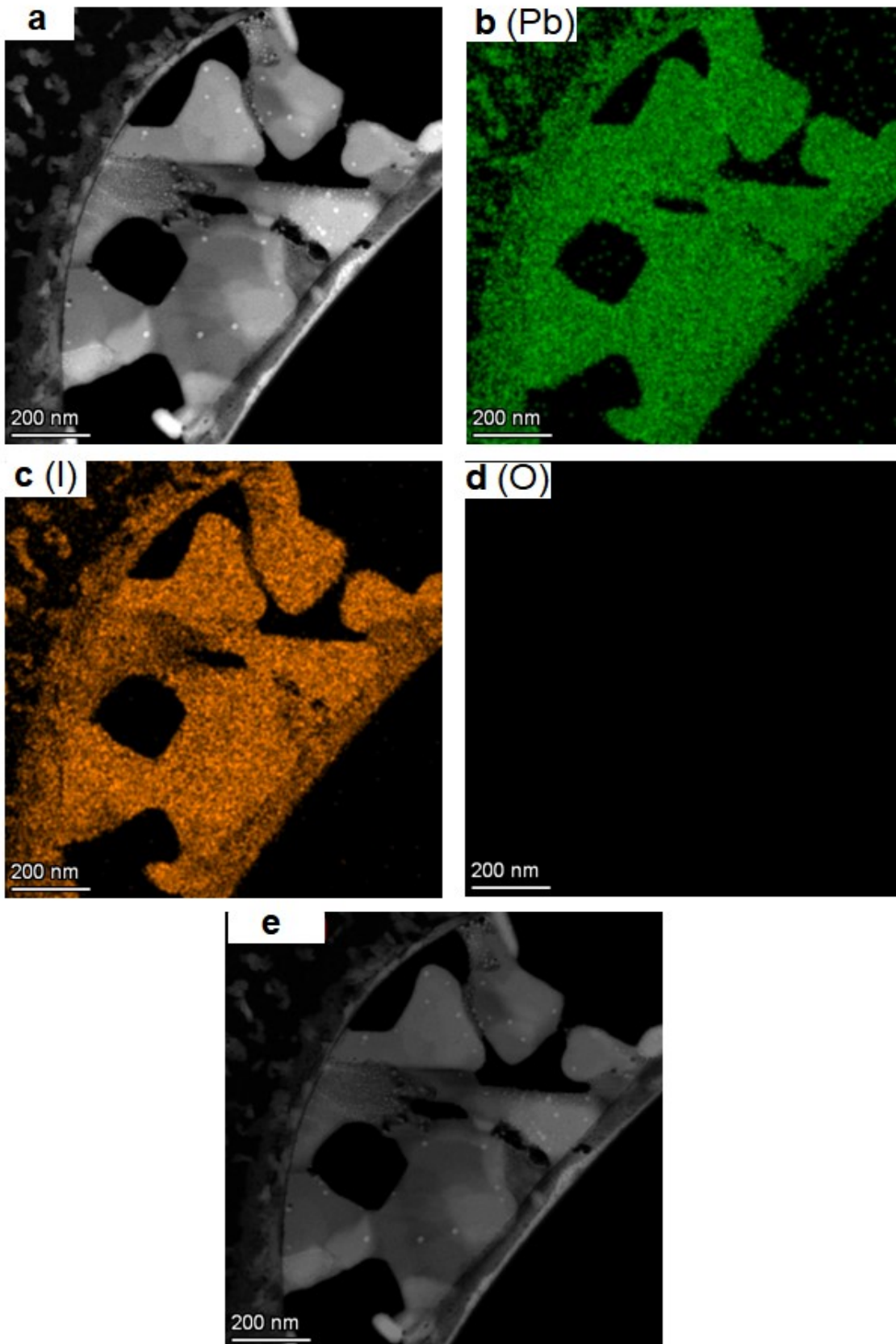
Fig. S24. HAADF STEM **(a)** and STEM-EDS data **(b – d)** measured for perovskite grains deposited from a dilute perovskite solution (0.28 M). **(e)** A composite colour map that overlays the oxygen elemental STEM-EDS data (d) with the STEM image (a).
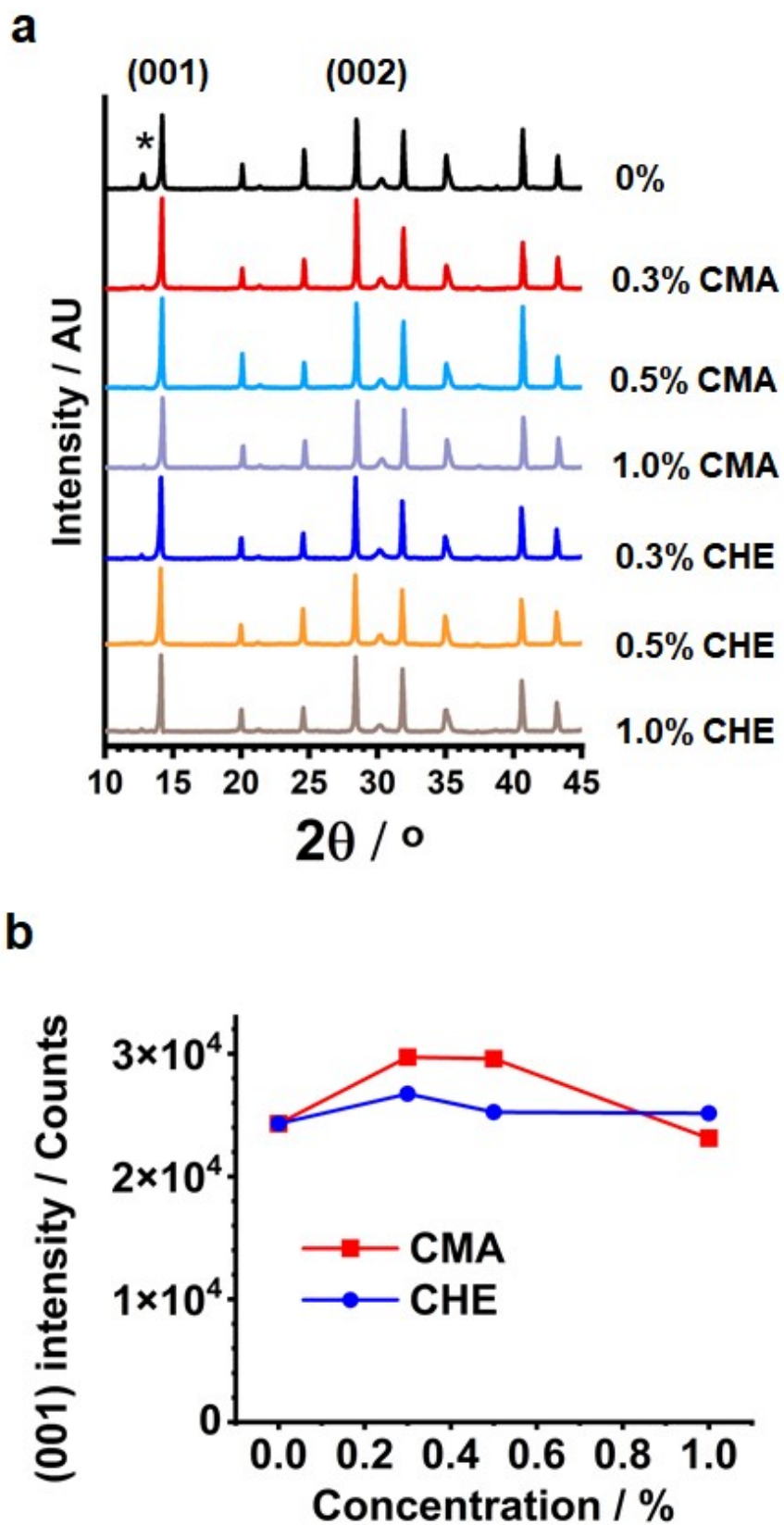
Fig. S25. (a) X-ray diffraction patterns for the perovskite films containing different concentrations of CMA or CHE (shown). The asterisk indicates PbI_2. **(b)** Variation of the scattered intensity of (001) peak from (a) with additive concentration.
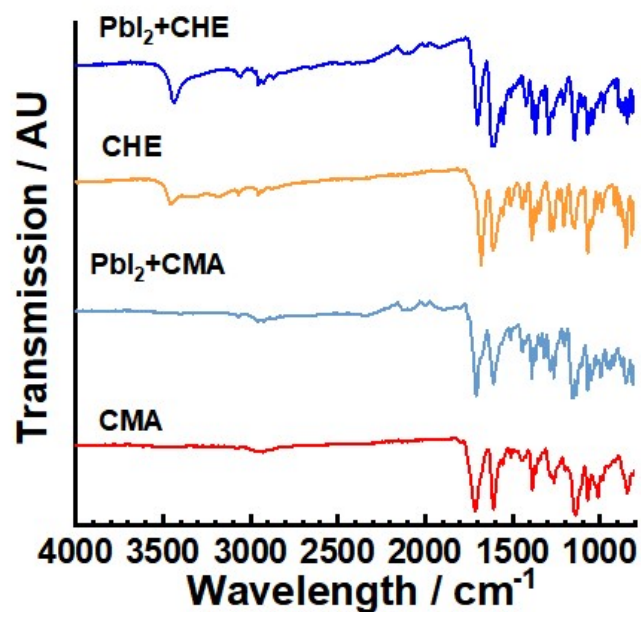
Fig. S26. FTIR spectra for CMA and CHE and also their mixtures with PbI$_2$.

Applying Student's t-test to the J_{sc} data

We applied the independent two-sample t-test to the J_{sc} data using[3]

$$t = \frac{\overline{x_1} - \overline{x_2}}{\sqrt{\left(\dfrac{s_1^2}{n_1} + \dfrac{s_2^2}{n_2}\right)}} \qquad \text{(S1)}$$

where x_1 and x_2 are the sample means for sample set 1 and 2, respectively. The values for s_1 and s_2 are the respective standard deviations. The values for t calculated for the J_{sc} data from the *same* sweep directions and the values for a threshold probability (P) value of 0.05 are compared. The latter value is derived from the TDIST function in Excel[4]. The data for each CMA and CHE *J-V* sweep are compared in Table S6. There are three concentrations where the CMA and CHE concentrations are the same: 0.3, 0.5 and 1.0%. There are two sweep directions for each set of data (forward and reverse). The data show that for 5 out of the 6 Student t-tests the calculated t values are less than the P = 0.05 threshold. For only one test sample (0.5% reverse sweep) is the null hypothesis proved at P = 0.05. However, the null hypothesis is disproved when P = 0.10 (see Table S6). Therefore, we conclude that the J_{sc} values for the CMA-based devices *are significantly higher* than those for the CHE-based devices.

Estimation of the number of CHE and CMA layers on the perovskite grains

In the following we use a simple geometric argument to provide "ball park" estimates of the maximum number of CHE and CMA layers on the perovskite grains for the devices studied in this study. To do this we first calculate the mass of CAA present for each grain of perovskite deposited. The mass ratio of CAA to perovskite deposited ($m_{CAA(dep)}/m_{PVK(dep)}$) via spin-coating is assumed to be the same as the mass ratio of CAA and perovskite precursors initially present in the solution used for spin-coating ($m_{CAA(init)}/m_{PVK(Pre)}$), i.e.,

$$\frac{m_{CAA(dep)}}{m_{PVK(dep)}} = \frac{m_{CAA(init)}}{m_{PVK(Pre)}} \qquad \text{(S2)}$$

From the masses of the perovskite precursors used given in the Experimental section the value of $m_{CAA(dep)}/m_{PVK(dep)}$ for the 0.3% CHE and CMA solutions is 6.3 x 10^{-3}.

We next calculate the mass of perovskite for a nominal cubic grain with a unit length, l, of 500 nm within the film as depicted in Fig. S27. Accordingly, the calculated grain volume is 1.3 x 10^{-13} cm^3. The perovskite (cubic) grain mass is 5.3 x 10^{-13} g using a perovskite density of[5] 4.1 g cm^{-3}. This gives a value for $m_{CAA(dep)}$ for that grain of 3.4 x 10^{-15} g using Equation S2. The total surface area of the grain is 1.5 x 10^{-8} cm^2. Assuming the CAA is equally spread over all six faces of the grain the calculated surface coverage is calculated as 0.23 µg cm^{-2}. It is noted that four of the faces of the grains are shared laterally with adjacent grains (Fig. S27) and have a surface coverage of 0.46 µg cm^{-2}. It is the top and bottom surface with a surface coverage (σ_{TB}) of 0.23 µg cm^{-2} that are most important for charge transport to the electrodes.
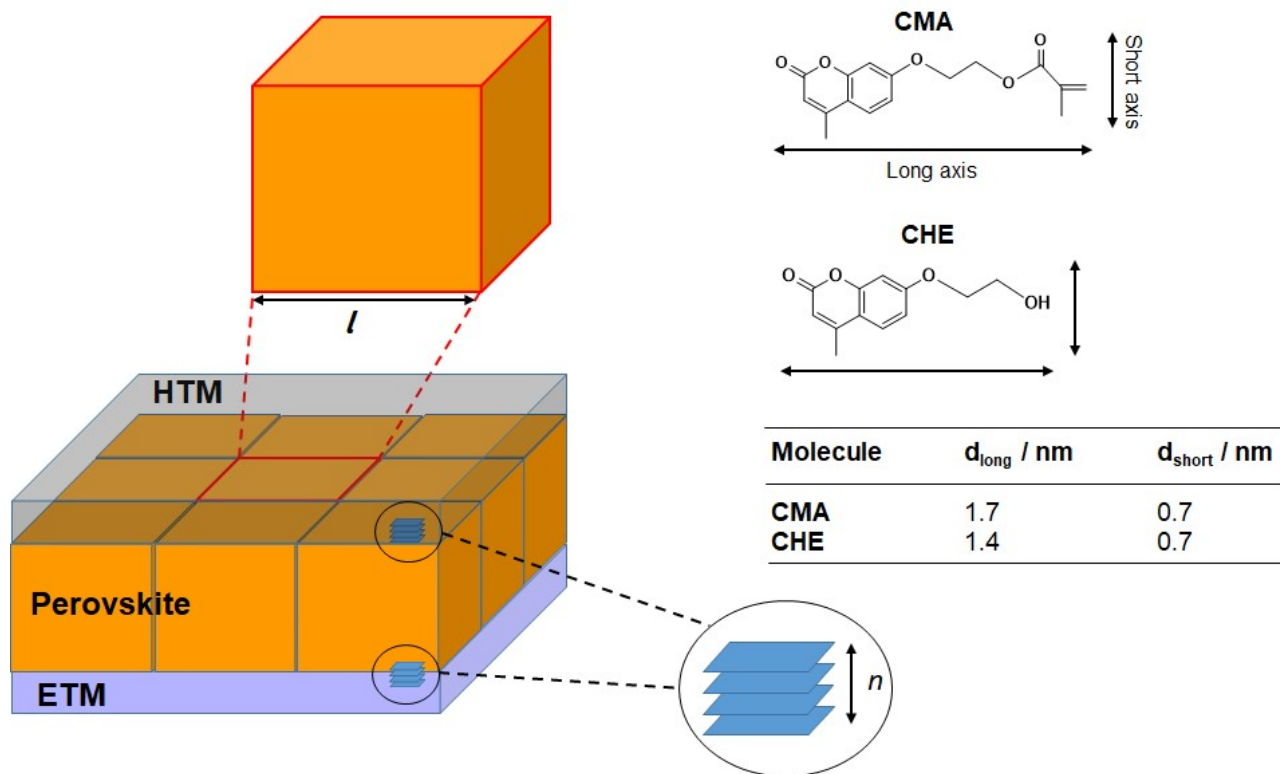
Fig. S27. Depiction of a nominal perovskite film composed of cubic grains. The CAAs (CHE and CMA) are assumed in this simplified model to stack as depicted at all of the grain boundaries.

We next calculate mass per unit area values for the CMA and CHE molecules. These values will subsequently be used to estimate of the number of CAA layers at the grain boundaries as shown below. The cross-sectional area of the CMA and CHE molecules are calculated from their structures (Fig. S27) to be $\approx 1.2 \times 10^{-14}$ cm^2 and 1.0×10^{-14} cm^2, respectively. The masses of one CMA and one CHE molecule are calculated as 4.8×10^{-16} µg and 3.7×10^{-16} µg, respectively, from their molecular weights of 288 g mol^{-1} and 220 g mol^{-1} using Avogadro's number. It follows that the mass per unit area values for CMA and CHE are both equal to ≈ 0.04 µg cm^{-2}. Therefore, a perfect monolayer of CMA and CHE molecules with no gaps between the molecules would have a surface coverage of (σ_m) 0.04 µg cm^{-2}. It follows from the value of σ_{TB}/σ_m (= 5.75). Hence, for a 0.3% concentration of CMA and CHE this model suggests that there are $n \approx 6$ layers of each CAA at the interface between the top and bottom surfaces and the HTM and ETM, respectively.

The SEM images for Fig. S11 and Fig. S14 show that there are a range of grain sizes which will

increase the total surface area of the grains. Consequently, the value for *n* calculated above is a maximum value. Furthermore, the calculations above assume that CMA and CHE are planar both at the interface and in subsequent layers. The modelling from Fig. 4 shows that the first layer is not completely planar and we have no modelling data for subsequent layers. Therefore, the above calculated number of layers is a ball-park estimate only. This analysis supports the view that there are multiple layers of each additive at the perovskite surfaces.

Table. S1 Photovoltaic parameters measured for the PSCs in this study.

System	Scan direction	V_{oc} (V)	J_{sc} (mA.cm^{-2})	FF (%)	PCE (%)	HI (%)[a]
0	Forward	1.09±0.024	22.8±0.35	68.36±2.35	17.0±0.66	6.3
	Reverse	1.10±0.023	22.8±0.36	72.62±1.31	18.14±0.35	
	Average	1.09±0.023	22.77±0.35	70.49±1.37	17.53±0.37	
	Best	**1.12**	**23.19**	**73.7**	**19.15**	
0.3%CMA	Forward	1.14±0.010	23.67±0.39	72.91±1.03	19.69±0.54	2.0
	Reverse	1.15±0.008	23.66±0.39	74.16±0.85	20.09±0.48	
	Average	1.14±0.009	23.66±0.39	73.53±0.83	19.89±0.49	
	Best	**1.15**	**24.36**	**75.71**	**21.28**	
0.5%CMA	Forward	1.13±0.007	23.35±0.36	71.45±1.18	18.92±0.42	1.6
	Reverse	1.14±0.007	23.30±0.35	72.47±0.70	19.23±0.33	
	Average	1.14±0.007	23.33±0.35	71.96±0.86	19.07±0.36	
	Best	**1.14**	**23.93**	**73.18**	**20.02**	
1.0%CMA	Forward	1.06±0.04	22.69±0.49	62.7±2.7	15.04±0.39	9.1
	Reverse	1.08±0.033	22.66±0.47	67.71±2.8	16.54±0.5	
	Average	1.07±0.037	22.67±0.49	65.21±2.74	15.79±0.39	
	Best	**1.08**	**23.06**	**70.73**	**17.54**	
0.3%CHE	Forward	1.13±0.016	23.29±0.4	72.81±1.36	19.18±0.85	4.0
	Reverse	1.14±0.012	23.27±0.4	75.34±0.70	19.97±0.58	
	Average	1.13±0.014	23.28±0.41	74.07±0.89	19.58±0.70	
	Best	**1.16**	**23.86**	**76.61**	**21.14**	
0.5%CHE	Forward	1.11±0.014	23.11±0.45	68.17±2.04	17.44±0.72	11
	Reverse	1.13±0.010	23.11±0.44	75.29±0.74	19.66±0.37	
	Average	1.12±0.012	23.11±0.44	71.73±1.06	18.55±0.46	
	Best	**1.14**	**23.78**	**75.56**	**20.51**	
1.0%CHE	Forward	1.03±0.03	22.35±0.42	56.0±3.24	12.88±1.0	21
	Reverse	1.08±0.02	22.34±0.38	67.65±1.54	16.31±0.32	
	Average	1.05±0.026	22.34±0.40	61.83±1.89	14.59±0.57	
	Best	**1.1**	**22.24**	**69.24**	**16.83**	

[a] HI = 100 x (PCE$_{REV}$ – PCE$_{FWD}$)/PCE$_{REV}$

Table S2. PSC efficiencies reported for devices based on similar perovskite structure- ETL/triple

cations perovskites (CsFAMAPbIBr)/Spiro-OMeTAD/Electrode to that used in the present study.

Structure	Voc / V	Jsc / mA/cm^2	FF / %	PCE / %	Ref.
ITO/CSCO@KCl/Perovskite/Spiro-OMeTAD/Au	1.18	24.03	78.33	22.21	6
FTO/SnO$_2$-ETL/Perovskite/Spiro-OMeTAD/Au	1.16	22.40	78	20.5	7
FTO/SnOx/(Perovskite:oxo-G/DA)/Spiro-OMeTAD/Au	1.13	23.1	81	21.1	8
ITO/SnO$_2$/ Perovskite /Spiro-OMeTAD+FG/Au	1.17	23.99	78.11	21.92	9
FTO/C-TiO$_2$/mp-TiO$_2$ /Perovskite/QDs/Spiro-OMeTAD/Au	1.14	23.35	79	21.14	10
FTO/SnO$_2$/Perovskite/TFMBA/Spiro-OMeTAD/Au	1.177	22.75	76.8	20.56	11
ITO/SnO$_2$/SAM/ Perovskite /Spiro-OMeTAD/Au	1.185	23.26	77.8	21.44	12
ITO/SnO$_2$/triazole-alloyed Perovskite /Spiro-OMeTAD/Au	1.09	24.4	79.0	20.9	13
FTO/TiO$_2$/Perovskite-PAA/Spiro-OMeTAD/Au	1.207	23.75	77.53	22.23	14
FTO/TiO$_2$/Perovskite/PFTS-10/spiro-OMeTAD/Au	1.176	23.03	78.80	21.34	15
ITO/SnO$_2$/Perovskite/PBTFO HTM/Au	1.22	23.0	78.9	22.1	16
ITO/NH$_2$-TiO$_2$/PVK/spiro-OMeTAD/Au	1.19	23.39	76.60	21.33	17
FTO/TiO$_2$/BP/PVK/BP/Spiro-OMeTAD/Ag	1.12	23.86	73.82	19.83	18
ITO/SnO$_2$/PVK-TPFPB/Spiro-OMeTAD/Au	1.16	23.74	77.8	21.42	19
ITO/SnO$_2$/PVK EA-Hex/spiro-oMeTAD/Ag	1.15	23.42	74.48	20.06	20
FTO/SnO$_2$/PVK-11MA/Spiro-OMeTAD/Au	1.16	24.70	81.40	23.34	21
ITO/SnO$_2$/Perovskite -CMA/Spiro-OMeTAD/Au	1.15	24.36	75.71	21.28	This work

Table S3 Fitting parameters from TRPL spectra of perovskite films prepared with different concentrations of CMA and CHE[a].

Sample	τ_1 (ns)	A_1 (%)	τ_2 (ns)	A_2 (%)	τ_{avg} (ns)
0%	10.6	3.07	127	96.93	126
0.3% CMA	50.0	1.30	258	98.70	257
0.5% CMA	58.6	4.41	216	95.59	213
1.0% CMA	23.2	2.79	175	97.21	174
0.3% CHE	78.1	9.03	186	90.97	182
0.5% CHE	73.8	9.69	135	90.31	132
1.0% CHE	60.9	18.07	132	81.93	120
0%[b]	49.5	7.34	179	92.66	175
0.3% CMA[b]	73.5	1.03	558	98.97	557
0.3% CHE[b]	56.5	2.53	287	97.47	286

[a] The parameters in the second column to the fourth column were calculated using equation 1. A_1 and A_2 represent relative amplitudes, τ_1 represents the decay time for fast charge carrier quenching and τ_2 represents the decay time for the slow decay process (see main text). τ_{avg} was calculated using equation 2. Unless otherwise stated, the films were deposited on glass/ITO/SnO_2 and the light was incident from the film side. [b] These films were deposited on glass and the light was incident from the glass side.

Table S4. Calculated relative energies of the CMA configurations investigated *before* binding to perovskite[a]

Configuration	Relative energy
I	0.17
II	0.04
III	0.03
IV	0.15
V	0.06
VI	0.00

[a] The relative energies are shown in eV per formula unit and are given with respect to the lowest energy calculated for CMA. The conformations are shown in Fig. S20.

Table S5. Calculated relative energies of the coumarin configuations investigated[a]

Configuration	CMA		CHE	
	PbX termination	AX termination	PbX termination	AX termination
1	0.28	0.00	0.52	0.21
2	0.00	0.03	0.00	0.00
3	1.12	0.47	1.17	0.60
4	0.92	0.71	1.02	0.74
5	1.02	0.54	1.20	0.66

[a] The relative energies are shown in eV per formula unit and are given with respect to the lowest energy calculated for CMA and CHE on perovskite surface with PbX or AX termination. X represents I and / or Br; whereas, A corresponds to FA and/or Cs.

Table S6. Students t-test analysis for the J_{sc} data measured in this study.

Test	J_{sc} data	DF^a	t	$P (0.05)^b$	Null hypothesis^c
1	0.3% Fwd	58	3.6383	6 x 10^{-4}	Disproved
2	0.3% Rev	58	3.7766	4 x 10^{-4}	Disproved
3	0.5% Fwd	58	2.3882	0.0202	Disproved
4	0.5% Rev	58	1.8623	0.0676	Disproved^d
5	1.0% Fwd	46	2.5474	0.0143	Disproved
6	1.0% Rev	46	2.6309	0.0115	Disproved

^{a} Degree of freedom. ^{b} The threshold for $t_{0.975}$ is 0.05 unless otherwise stated. ^{c} The null hypothesis is that there is no difference between the J_{sc} data measured for the CMA and CHE devices. ^{d} The hypothesis for this data set was *proved* at P = 0.05. However, it was *disproved* at $t_{0.95}$ which corresponds to $P = 0.10$.

References

1.   R. Xia, X.-X. Gao, Y. Zhang, N. Drigo, V. I. E. Queloz, F. F. Tirani, R. Scopelliti, Z. Huang, X. Fang, S. Kinge, Z. Fei, C. Roldán-Carmona, M. K. Nazeeruddin and P. J. Dyson, *Adv. Mater.*, 2020, **32**, 2003801.

2.   H. Zhang, Z. Chen, M. Qin, Z. Ren, K. Liu, J. Huang, D. Shen, Z. Wu, Y. Zhang, J. Hao, C.-s. Lee, X. Lu, Z. Zheng, W. Yu and G. Li, *Adv. Mater.*, 2021, **33**, 2008487.

3.   E. R. Ziegel, *Technometrics*, 2004, **46**, 498.

4.   Formula syntax and usage of the TDIST function in Microsoft Excel., https://support.microsoft.com/en-us/office/tdist-function-630a7695-4021-4853-9468-4a1f9dcdd192).

5.   C. C. Stoumpos, C. D. Malliakas and M. G. Kanatzidis, *Inorg. Chem.*, 2013, **52**, 9019-9038.

6.   F. Li, Z. Shen, Y. Weng, Q. Lou, C. Chen, L. Shen, W. Guo and G. Li, *Adv. Funct. Mater.*, 2020, **30**, 2004933.

7.   Q. Dong, J. Li, Y. Shi, M. Chen, L. K. Ono, K. Zhou, C. Zhang, Y. Qi, Y. Zhou and N. P. Padture, *Adv. Energy Mater.*, 2019, **9**, 1900834.

8.   M. Li, W.-W. Zuo, Q. Wang, K.-L. Wang, M.-P. Zhuo, H. Köbler, C. E. Halbig, S. Eigler, Y.-G. Yang, X.-Y. Gao, Z.-K. Wang, Y. Li and A. Abate, *Adv. Energy Mater.*, 2020, **10**, 1902653.

9.   Q. Lou, G. Lou, H. Guo, T. Sun, C. Wang, G. Chai, X. Chen, G. Yang, Y. Guo and H. Zhou, *Adv. Energy Mater.*, 2022, **12**, 2201344.

10.   S. Akin, Y. Altintas, E. Mutlugun and S. Sonmezoglu, *Nano Energy*, 2019, **60**, 557-566.

11.   J. Li, T. Bu, Z. Lin, Y. Mo, N. Chai, X. Gao, M. Ji, X.-L. Zhang, Y.-B. Cheng and F. Huang, *Chem. Eng. J.*, 2021, **405**, 126712.

12.   Z. Dai, S. K. Yadavalli, M. Chen, A. Abbaspourtamijani, Y. Qi and N. P. Padture, *Science*, 2021, **372**, 618-622.

13.   J. Kim, A. J. Yun, B. Gil, Y. Lee and B. Park, *Adv. Funct. Mater.*, 2019, **29**, 1905190.

14.   W. Zhao, P. Guo, J. Su, Z. Fang, N. Jia, C. Liu, L. Ye, Q. Ye, J. Chang and H. Wang, *Adv. Funct. Mater.*, 2022, **32**, 2200534.

15.   P. Guo, Q. Ye, C. Liu, F. Cao, X. Yang, L. Ye, W. Zhao, H. Wang, L. Li and H. Wang, *Adv. Funct. Mater.*, 2020, **30**, 2002639.

16.   Z. Li, J. Park, H. Park, J. Lee, Y. Kang, T. K. Ahn, B.-G. Kim and H. J. Park, *Nano Energy*, 2020, **78**, 105159.

17.   W. Hu, W. Zhou, X. Lei, P. Zhou, M. Zhang, T. Chen, H. Zeng, J. Zhu, S. Dai and S. Yang, *Adv. Mater.*, 2019, **31**, 1806095.

18.   M. Zhang, M. Ye, W. Wang, C. Ma, S. Wang, Q. Liu, T. Lian, J. Huang and Z. Lin, *Adv. Mater.*, 2020, **32**, 2000999.

19.   J. Jia, J. Dong, B. Shi, J. Wu, Y. Wu and B. Cao, *ACS Applied Materials & Interfaces*, 2021, **13**, 2472-2482.

20.   H. B. Lee, M. K. Jeon, N. Kumar, B. Tyagi and J. W. Kang, *Advanced Functional Materials*, 2019, **29**, 1903213.

21.   L. Zhu, X. Zhang, M. Li, X. Shang, K. Lei, B. Zhang, C. Chen, S. Zheng, H. Song and J. Chen, *Advanced Energy Materials*, 2021, **11**, 2100529.